Research Square

Preprints are preliminary reports that have not undergone peer review.
They should not be considered conclusive, used to inform clinical practice,
or referenced by the media as validated information.

Spatial Characterization of Tray-Dependent Beam Structure and Exploratory Corner Geometry in a Preclinical Irradiator

Bashayr Alotaibi[1]
University of Alabama at Birmingham
Will Ren[2]
Hoover High School
Olebile Dikago[1]
University of Alabama at Birmingham
Ara Alexandrian[3]
Mary Bird Perkins Cancer Center
Joseph Steiner[4]
University of Chicago
Remo George
remogeorge@uab.edu
University of Alabama at Birmingham

Research Article

Keywords: X-RAD 320, orthovoltage irradiator, beam characterization, radiochromic film, field edge geometry, preclinical irradiation

Posted Date: November 9th, 2026

DOI: https://doi.org/10.21203/rs.3.rs-11109323/v1

License: This work is licensed under a Creative Commons Attribution 4.0 International License.
Read Full License

Additional Declarations: No competing interests reported.

Spatial Characterization of Tray-Dependent Beam Structure and Exploratory Corner Geometry in a Preclinical Irradiator

Bashayr Alotaibi[1], Will Ren[2], Bonny Dikago[1], Ara Alexandrian[3], Joseph Steiner[4], and Remo George[1]*

[1] Nuclear Medicine and Molecular Imaging Sciences Program, Department of Clinical and Diagnostic Sciences, School of Health Professions, University of Alabama at Birmingham, Birmingham, AL, USA

[2] Hoover High School, Hoover, AL, USA

[3] Department of Medical Physics, Mary Bird Perkins Cancer Center, Baton Rouge, LA, USA

[4] Department of Radiology, University of Chicago, Chicago, USA

*Corresponding author:

Remo George, Ph.D.
Nuclear Medicine and Molecular Imaging Sciences Program,
Department of Clinical and Diagnostic Sciences
School of Health Professions
University of Alabama at Birmingham
Birmingham, AL, USA
Email: remogeorge@uab.edu
ORCID: https://orcid.org/0000-0003-3108-2056

Keywords: X-RAD 320; orthovoltage irradiator; beam characterization; radiochromic film; field edge geometry; preclinical irradiation

ABSTRACT

Spatial characterization of cabinet irradiators supports reproducible irradiation of biological specimens. We evaluated central and peripheral field characteristics of an X-RAD 320 at upper and lower tray positions. Ionization-chamber measurements across two-dimensional grids assessed dose profiles, surfaces, isodose distributions, flatness, symmetry, and centering. One EBT-XD radiochromic film was separately irradiated at each of four corner positions. Horizontal, vertical, and diagonal gray value profiles were fitted with Gompertz functions to locate the 80%, 50%, and 20% normalized response positions and assess transition width and apparent corner geometry. Our results showed that the upper tray produced a higher, more compact central dose region, whereas the lower tray produced a lower, broader field, with approximate plateau dimensions of 20 × 20 cm and 30 × 30 cm, respectively. Flatness and symmetry changed little across the inner 20–60% evaluation windows but rose markedly in the 80% and 100% windows as field boundaries were incorporated. Field-center displacement occurred predominantly along the negative Y-axis, with upper- and lower-tray offsets of −3.76 and −3.17 cm. X-direction offsets were comparable to the uncorrected 0.65-cm separation between chamber alignment and reference points and total offsets were approximately 3.8 and 3.3 cm. Film transition widths ranged from 2.13 to 7.41 mm and were generally wider at the lower tray. Exploratory ratios suggested square-leaning upper corners and arc-leaning lower corners. Central profiles alone did not fully characterize the fields and tray position and specimen placement should therefore be considered, particularly near field boundaries.

INTRODUCTION

The X-RAD 320 is a self-shielded, cabinet-style orthovoltage irradiator designed for the irradiation of small animals, cell cultures, and other biological specimens. It produces polyenergetic kilovoltage X-rays at tube potentials up to 320 kV and allows specimens to be placed at different distances from the source using an adjustable irradiation tray (Precision X-Ray 2022). Its enclosed design allows irradiation to be performed in a laboratory without the requirement for additional radiation shielding. At our institution, this irradiator was previously used to establish a mouse model of cutaneous radiation syndrome, in which irradiation of the dorsal skin was documented using ionization-chamber and radiochromic-film measurements (Mujahid et al. 2025). That application provided direct motivation for the more detailed, unit-specific spatial characterization undertaken in the present study.

Reproducible radiobiological experiments require accurate knowledge of the dose magnitude and spatial distribution at the position of the specimen (Desrosiers et al. 2013). The spatial properties of an orthovoltage beam are influenced by the X-ray tube, focal-spot size, filtration, collimator geometry, source-to-specimen distance, and surrounding scattering materials (Khan and Gibbons 2014). Moving the x-ray source to irradiation tray distance changes the geometric projection of the beam and can alter the field size, dose magnitude, and edge transition. Beam profiles are commonly described using flatness and symmetry. Flatness describes dose variation within the central region of the field, whereas symmetry compares paired dose values at equal distances on opposite sides of the field center. The dosimetric gray value transition is commonly defined as the distance between the 80% and 20% dose positions across a field boundary. Radiochromic film is useful for examining such boundaries because it provides high spatial resolution and undergoes a measurable optical density change following radiation exposure, which can be described as a film gray value transition (Niroomand-Rad et al. 2020).

Several studies have characterized the X-RAD 320 using conventional dosimetric methods. Azimi et al. examined field sizes from 4 × 4 to 20 × 20 cm² and evaluated output, percentage depth dose, beam profiles, scatter factors, flatness, and symmetry using ionization-chamber measurements and Monte Carlo simulations (Azimi et al. 2015). Differences in flatness and symmetry were reported between the principal measurement axes and among field sizes. Pidikiti et al. characterized an X-RAD 320 X-ray source equipped with a custom collimation and image-guidance system that produced fields from 1 to 10 mm for stereotactic small-animal irradiation (Pidikiti et al. 2011). Aldelaijan et al. used EBT2 radiochromic film to evaluate output, depth-dose distributions, and beam profiles for biological specimens irradiated in air and under different scattering conditions (Aldelaijan et al. 2013). These studies established important dosimetric properties of the X-RAD 320 but did not specifically examine the local geometry at the intersections of adjacent field edges.

Characterization studies of other cabinet and small-animal irradiators have also shown that dose delivery can depend on machine configuration and experimental setup. Saikkonen et al. commissioned a MultiRad 350 system using radiochromic film, ionization chambers, and radiophotoluminescence dosimeters (Saikkonen et al. 2019). Bucher et al. demonstrated that specimen position, surrounding materials, and irradiation configuration can influence field and dose homogeneity in an X-ray cabinet (Bucher et al. 2021). More recently, Trompier et al. emphasized the need for detailed reporting of irradiator properties, irradiation geometry, and dosimetry methods in preclinical radiobiology (Trompier et al. 2024). These reports support unit-specific spatial characterization but do not provide an established method for describing corner shape in broad orthovoltage fields.

Within the literature reviewed for this study, no previous X-RAD 320 investigation was identified that combined whole field chamber-grid measurements at two tray positions with targeted film analysis at selected field corners. The purpose of the present study was therefore to characterize the central and peripheral field properties of an X-RAD 320 at its upper and lower irradiation tray positions. Chamber measurements were used to examine beam profiles, two- and three-dimensional dose distributions, flatness, symmetry, and field centering. Radiochromic film measurements were then used to examine normalized gray value transitions at four selected corner positions using horizontal, vertical,

and diagonal profiles. Idealized geometric ratios and three-point circle construction were applied as exploratory methods for describing apparent corner shape. This combined approach was intended to determine whether spatial characteristics observed near the field center adequately represented those found near the evaluated field edges and corners.

MATERIALS AND METHODS

Irradiator Setup & Dose Measurements

All measurements were performed using an X-RAD 320 cabinet irradiator (Precision X-Ray, North Branford, CT, USA). All chamber and film measurements were performed using the same manufacturer-supplied transparent polymer tray. The composition and thickness of the transparent tray were not independently verified. The irradiator was operated at 320 kVp and 12.5 mA. The beam passed through a 3 mm beryllium window and the 2 mm aluminum F1 filter. These tube voltage, tube current, and filtration settings were unchanged between the upper and lower tray measurements. The irradiator's integrated adjustable collimator was set to maximum field size for all measurements and was also not changed between the upper and lower tray positions. The physical dimensions and internal geometry of the collimator opening were not independently measured due to inaccessibility. The resulting spatial extent of the radiation field was characterized from the measured dose distributions.

Dose measurements were collected in air using a PTW Farmer 30013 ionization chamber connected to a PTW UNIDOS E dosimeter. The chamber and dosimeter were maintained under routine institutional calibration. Measurements were obtained with the chamber positioned directly on the irradiation tray. Consequently, possible scatter and backscatter from the tray and cabinet were included in the measured values. The chamber was placed horizontally on each irradiation tray, with the X-ray beam incident on the side of the chamber. The vertical distance from the X-ray tube housing to the chamber measurement plane was 19.5 cm for the upper tray and 46 cm for the lower tray. These distances were measured at the position identified by the illuminated cross-hairs and should not be interpreted as focal-spot-to-chamber distances.

Each tray was covered with paper marked with grid lines at 1 cm intervals along the X- and Y-axes. The coordinate origin was placed at the lower-left corner of the cabinet, and the grid extended from 0 to 70 cm along both axes. The recorded measurement positions generally extended from 0 to 70 cm. Measurements were normally collected at approximately 5 cm intervals. Additional points were measured at or near 1 cm intervals in regions where the dose changed rapidly from the high-dose plateau to background.

At each position, the midpoint between the chamber tip and its manufacturer-defined reference point was aligned with the selected grid mark. The long axis of the chamber was maintained in the same direction whenever possible. At some peripheral grid positions adjacent to the cabinet wall, the chamber was rotated by 180° because the available space prevented placement in its original orientation. This rotation was required only at positions outside the central irradiated region, where the measured values were at or near background. These measurements were used to document the return of the field profile to background. The possible effect of chamber orientation was not evaluated separately, however, because the rotation was limited to background-level positions, it was not expected to significantly affect the reported central field dose, flatness, symmetry, or centering measurements. The grid coordinates used for the field centering analysis were not corrected for the 6.5 mm distance between the chamber alignment point and the manufacturer defined reference point.

Three readings were collected at each measurement position, and their mean was used for analysis. Measurements were obtained under stable environmental conditions at approximately 22°C and 101 kPa. The values displayed by

the dosimeter were recorded in Gy. No additional temperature, pressure, polarity, or spatial-position corrections were applied because the main objective was to compare the relative spatial dose distribution under the same measurement conditions.

Central Axis Dose Profiles

The central-axis dose profiles shown in Fig. 1 were measured in a separate experiment from the three-dimensional dose measurements. Horizontal and vertical profiles were collected along the midlines of the X- and Y-axes for both the upper and lower trays. Each measurement used a 1 minute irradiation (750 mAs). Measurements were collected at 5 cm intervals, with additional points collected near the field edges to better define the rapid dose transition. The mean dose in Gy was plotted against the physical distance coordinate along each axis. These independently measured profiles were used to display the one-dimensional variation in dose along the central X- and Y-axes. They were not used for the subsequent flatness, symmetry, or alignment calculations.

To provide a descriptive measure of profile width, the positions at which each profile crossed 50% of its own maximum measured dose were estimated on the rising and falling field edges by linear interpolation between adjacent measurement points. The distance between these two positions was reported as the full width at half maximum (FWHM). These FWHM values were calculated only for the independently measured profiles shown in Fig. 1 and were not used for the subsequent flatness, symmetry, alignment, or approximate plateau-dimension calculations.

Three-Dimensional Dose Mapping

The three-dimensional dose distributions shown in Fig. 2 were obtained in a separate grid-measurement experiment. A 30 s (375 mAs) irradiation was used at each selected grid position. Three readings were collected at each position, and the mean dose in Gy was entered into the corresponding grid location.

The X and Y coordinates and corresponding dose measurements were arranged as separate two-dimensional Excel matrices for the upper and lower trays, with X coordinates represented by columns and Y coordinates represented by rows. The matrices were imported into Python using pandas, converted to NumPy arrays, and used to generate X-Y coordinate grids with the NumPy meshgrid function. The measured doses were plotted without normalization or smoothing as three-dimensional Matplotlib surfaces using the plot_surface function and viridis colormap. Surface edge lines were omitted. The oblique viewing angle was selected separately for each tray to show the dose falloff at the lower field boundaries. These views were used for qualitative visualization only and quantitative comparisons were based on the underlying coordinate and dose measurements.

The approximate field dimensions were estimated from the spatial extent of the high-dose plateau in the three-dimensional dose matrices. The three-dimensional dose matrices were also used for the flatness, symmetry, and alignment calculations described below.

Isodose Contour Mapping

The isodose maps shown in Fig. 3 were generated from the same 30 s grid measurements used for the three-dimensional surfaces. The dose values available for analysis were recorded to two decimal places, corresponding to a retained numerical precision of 0.01 Gy. When more than one grid position shared the maximum recorded value at this precision, each position was marked as a 100% dose location. Additional isodose levels were calculated from 10% to 90% of the maximum in 10% increments. Each tray was normalized to its own maximum and contour maps were used to compare field shape and spatial distribution.

Filled color regions were generated using the Matplotlib contourf function. Black contour boundaries were added using the contour function. Contour boundaries were drawn between neighboring measurement positions. Equal scaling was used for the X- and Y-axes so that the field geometry was not distorted. The Y-axis was inverted to reproduce the orientation of the original measurement grid. Grid positions equal to the maximum measured dose were marked with a red star. Therefore, both tied maximum positions were marked in the upper tray map. The Python codes used to generate the three-dimensional dose surfaces and isodose contour maps are provided in Online Resources 1 and 2.

Beam Flatness & Symmetry Calculations

Beam flatness, symmetry, and field centering were calculated from the two-dimensional dose matrices used to generate Figs. 2 and 3. These calculations did not use the separately measured central-axis profiles shown in Fig. 1. For each tray, the horizontal profile was selected from the matrix row with the largest summed dose, and the vertical profile was selected from the column with the largest summed dose. For the upper tray, these profiles were obtained at Y = 30 cm and X = 40 cm, respectively. The columns at X = 35 and 40 cm had equal summed doses in the upper tray matrix. The X = 40 cm column was selected because it contained the maximum measured dose. For the lower tray, the horizontal and vertical profiles were obtained at Y = 35 cm and X = 35 cm, respectively.

For the flatness calculation (Fig. 4 a(i), b(i)), the full field width was defined for each tray and profile direction as the span between the first and last positions within the contiguous sequence of sampled locations where the measured dose exceeded 0.02 Gy. The same fixed absolute background threshold was applied to the upper and lower trays and was not normalized to their respective maximum doses. The outermost sampled coordinates meeting this condition defined the 100% flatness window. The midpoint between these coordinates was used as the center of the flatness window. Additional windows covering 80%, 60%, 40%, and 20% of the full width were constructed symmetrically around this center. When a window boundary occurred between measured coordinates, the dose at the boundary was estimated by linear interpolation. Flatness within each window was calculated as:

$$F\ (\%) = \frac{D_{max} - D_{min}}{D_{max} + D_{min}} \times 100\% \ ,$$

Where D_{max} and D_{min} were the maximum and minimum dose values within the evaluated window. A value closer to 0% represented a more uniform dose distribution.

For symmetry (Fig. 4 a(ii), b(ii)), the maximum dose in each profile was first identified. The positions at which the dose decreased to 50% of this maximum on the two sides of the profile were estimated by linear interpolation. The midpoint between these positions was defined as the dose-based profile center, c, and the distance between them was defined as the full width at half maximum (FWHM). The dose at the profile center, D_c, was also estimated by linear interpolation.

For each measured position on the higher-coordinate side of the profile center, its distance from the center, r, was calculated. The dose at the corresponding position on the opposite side, (c-r), was estimated by linear interpolation. Symmetry for each matched pair was calculated as:

$$S_{(r)}(\%) = \frac{\left|D_{(c+r)} - D_{(c-r)}\right|}{D_c} \times 100\%$$

Symmetry was evaluated within windows covering 100%, 80%, 60%, 40%, and 20% of the full width at half maximum. For each window, the maximum symmetry value among the eligible matched pairs was reported. A value

closer to 0% represented better symmetry. No symmetry value was reported when a window contained no eligible matched pair. For both analyses, the evaluation windows were nested, with each smaller window contained within the larger windows. Since flatness was calculated from the maximum and minimum values within each window and symmetry was reported as the maximum pairwise difference, expansion of the evaluation window could leave the reported value unchanged or increase it, but could not reduce it. The analysis therefore emphasized the window at which the principal increases occurred.

The FWHM-derived centers of the horizontal and vertical profiles were combined to define the dose-based field center, (X_b, Y_b). The physical center of the cabinet was located at (35, 35) cm. The horizontal and vertical offsets were calculated as ($\Delta X = X_b - 35$) and ($\Delta Y = Y_b - 35$), respectively. The total centering discrepancy was calculated as ($\sqrt{\Delta X^2 + \Delta Y^2}$). For display, shaded central reference regions measuring 20 × 20 cm for the upper tray (Fig. 4 a(iii)) and 30 × 30 cm for the lower tray (Fig. 4 b(iii)) were centered on the dose-based field centers.

Radiochromic Film Corner Measurements and Profile Fitting

A separate radiochromic film experiment was performed to examine the field edges at four selected corner positions: Lower Bottom-Left, Lower Top-Right (Fig. 5a), and Upper Bottom-Left, Upper Top-Right (Fig. 5b). This exploratory sampling design evaluated two diagonally opposed field corners at each tray position: the bottom-left and top-right corners of the upper tray field and the bottom-left and top-right corners of the lower tray field. The remaining two corners at each tray position were not sampled. The corner-film experiment was intended to provide an initial descriptive assessment rather than a complete characterization of every field corner.

A total of four Gafchromic EBT-XD film pieces (Ashland Advanced Materials, Bridgewater, NJ) were used, with one film positioned at each selected corner. The film dimensions varied slightly but were approximately 2 × 2 cm. The films were local samples of the field boundaries and were not intended to cover the complete radiation field. Each film was placed directly on the irradiation tray and was exposed during a separate irradiation using the beam settings described before, with an exposure time of 30 seconds. All measurements were treated as descriptive, with profiles obtained from different regions or directions on the same film treated as technical measurements and not independent replicates.

The films were scanned at 300 dots per inch, corresponding to a pixel size of 0.0847 mm. The scanned images were converted to 8-bit grayscale in ImageJ. The apparent field vertex, defined as the corner at which the horizontal and vertical boundaries of the darkened irradiated region met, was first identified on each scanned film image. Horizontal, vertical, and diagonal line profiles were then placed across the light-to-dark transition for each film, producing 12 profiles from four films. The horizontal, vertical, and diagonal lines were oriented at 0°, 90°, and 45°, respectively. Horizontal and vertical reference coordinates were positioned 90 pixels from the identified vertex. For the diagonal line, the coordinate displacement along each axis was scaled by $1/\sqrt{2}$ so that the total distance from the vertex was equal to that used for the horizontal and vertical lines. The calculated coordinates were entered into the ImageJ makeLine macro command to maintain consistent line placement and orientation. Gray values along each line were obtained using the Plot Profile function and exported as distance–gray-value data.

Each gray value profile was normalized between its measured dark and light plateaus. The dark plateau was assigned a normalized gray value of 0%, and the light plateau was assigned a value of 100%. Each normalized profile was fitted with a decreasing Gompertz sigmoid function. The fitted curve was used to identify the positions corresponding to 80%, 50%, and 20% of the normalized gray value range. The 50% position was used as an operational measure of the field edge location, and the distance between the 80% and 20% positions was used to characterize the width of the

film response transition. These percentages describe normalized film gray value and not percentage absorbed dose. The measured profiles, fitted curves, and threshold positions are shown in Fig. 5.

Film Response Transition Width

For each horizontal, vertical, and diagonal gray value profile, the positions corresponding to 80% and 20% of the normalized gray value range were obtained from the fitted Gompertz curve. The transition width was calculated as the absolute difference between these two positions. Pixel distances were converted to millimeters using the scanning resolution of 0.0847 mm per pixel:

$$\text{Transition width (mm)} = |x_{20} - x_{80}| \times 0.0847 \text{ mm/pixel}$$

where x_{20} and x_{80} were the pixel positions corresponding to the 20% and 80% normalized gray value levels, respectively. One field vertex was evaluated on each of the four films. One horizontal, one vertical, and one diagonal gray value profile was analyzed at each vertex, yielding three transition-width measurements per film and 12 transition-width measurements in total. The calculated values were displayed descriptively in Table 1.

Local Linear Fit of the Film-Response Transition

To describe the steepness of the film response transition, the measured data points between the 80% and 20% normalized gray value positions were isolated from each profile. An ordinary least squares linear regression was applied to normalized gray value as a function of distance using the Trendline function in Excel. The regression slope was converted from percentage gray value per pixel to percentage gray value per millimeter using the scanning resolution of 0.0847 mm per pixel. The coefficient of determination (R^2) was recorded to describe how closely the measurements within the isolated transition followed a linear relationship. Slopes were negative because the normalized gray value decreased as the profile crossed from the lighter region into the darker irradiated region. A larger absolute slope represented a steeper and narrower transition. The transition width, slope, and R^2 value for each profile were reported descriptively in Table 1. The individual regression plots for all 12 profiles are provided in Online Resource 3.

Exploratory Corner-Geometry Assessment

An exploratory geometric assessment was performed using the horizontal, vertical, and diagonal 20 - 80% normalized gray value transition widths of the four evaluated corner films. For each position, a corner geometry ratio was calculated as:

$$\text{Corner geometry ratio} = \frac{\text{diagonal transition width}}{\text{mean of the horizontal and vertical transition widths}}$$

Under the simplified geometric model used in this study, an ideal sharp 90° corner was expected to produce a ratio approaching $\sqrt{2}$, or approximately 1.41, because the diagonal transition extends across a greater geometric distance than the perpendicular transitions. An ideal rounded corner was expected to produce a ratio approaching 1.00 because the transition distance is similar in the horizontal, vertical, and diagonal directions. Each measured ratio was compared descriptively with these two reference values. Ratios closer to 1.41 were described as square-leaning, while ratios closer to 1.00 were described as arc-leaning. These reference values were used as exploratory geometric guides and not as validated shape classification cutoffs.

The horizontal, vertical, and diagonal 50% normalized gray value positions were also converted from pixels to millimeters and used to produce descriptive corner representations. For each position described as square-leaning, the X-coordinate of the horizontal profile 50% location and the Y-coordinate of the vertical profile 50% location were combined to define a derived H/V vertex. Dashed horizontal and vertical guide lines were drawn between the measured points and this derived vertex. The diagonal 50% location was plotted independently but was not used to determine the vertex, and no radius was assigned. These L-shaped representations were descriptive and were not fitted to all three 50% locations.

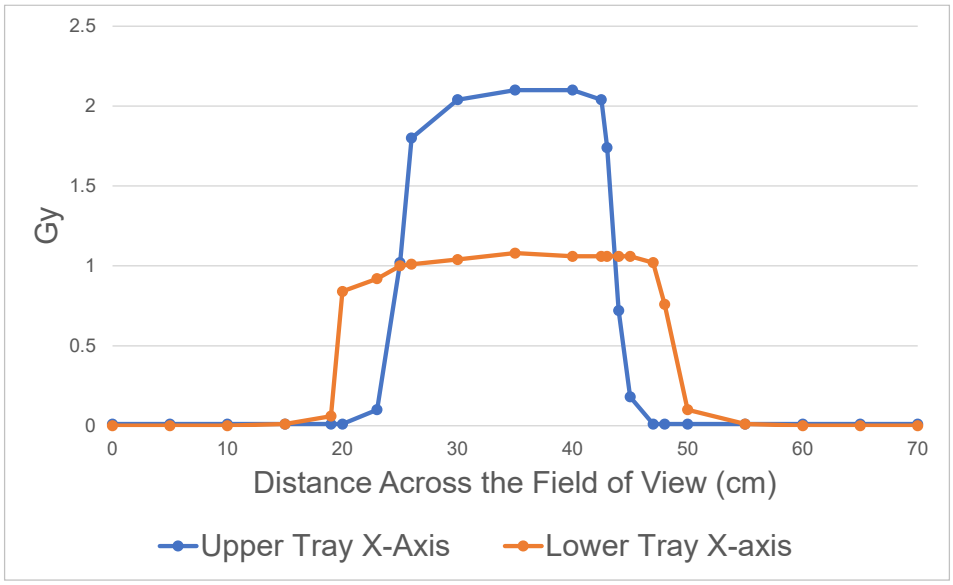
For each position described as arc-leaning, the unique circle passing through the horizontal, vertical, and diagonal 50% locations was constructed, and its radius was reported as a descriptive estimate of local curvature. Because any three non-collinear points mathematically define a circle, the circle construction was not used independently to establish that the complete field boundary followed a circular arc. All ratios and geometric representations were interpreted descriptively. The ratios, reference geometries, and descriptive corner representations are shown in Fig. 6.

RESULTS

Beam-profile measurements along the X-axis showed clear differences between the upper and lower irradiation trays (Fig. 1a). For the upper tray, the measured dose increased rapidly between approximately 23 and 30 cm. It reached a plateau of approximately 2.04–2.10 Gy between 30 and 42.5 cm and then decreased sharply to background levels by 47 cm. In comparison, the lower tray dose increased between approximately 19 and 25 cm and remained between approximately 1 and 1.08 Gy from 25 to 47 cm. It then decreased to 0.10 Gy at 50 cm and approached background levels by 55 cm.

Figure 1

a



b

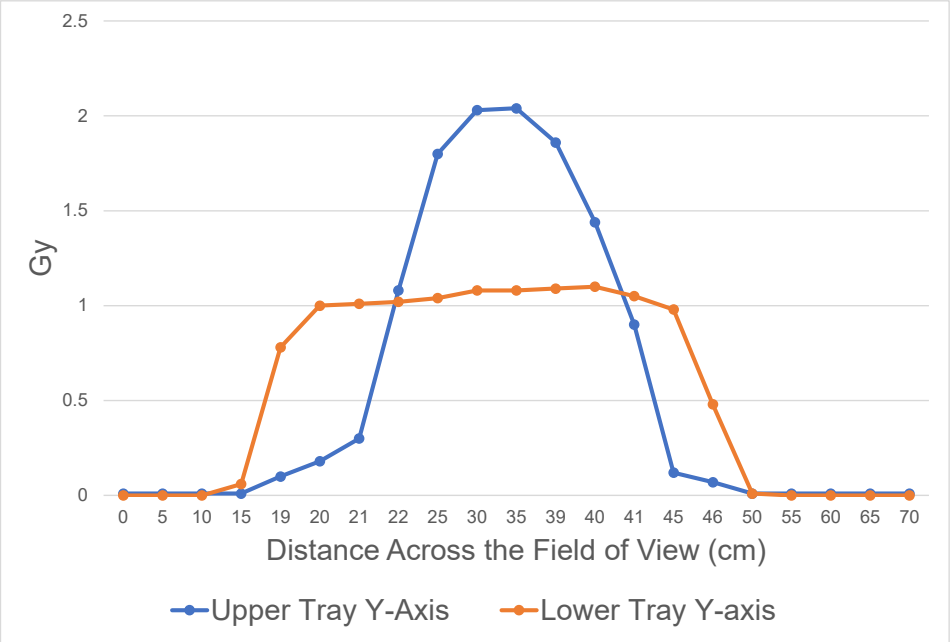


Fig. 1 Measured dose across the field. (a) X-axis and (b) Y-axis beam profiles for the upper and lower irradiation platforms, respectively, showing the measured dose across the field of view. The upper platform exhibits a central high dose plateau near 2 Gy, while the lower platform shows a broader region near 1 Gy. Both profiles return to near-zero dose at the field edges

The Y-axis profiles showed a similar difference between the two tray positions (Fig. 1b). The upper tray dose increased rapidly between approximately 21 and 30 cm and reached a maximum of approximately 2.04 Gy between 30 and 35 cm. The dose then decreased to background levels by 50 cm. The lower tray dose increased from 0.06 Gy at 15 cm to approximately 1 Gy at 20 cm. It remained between approximately 0.98 and 1.10 Gy from 20 to 45 cm before decreasing to background levels by 50 cm. Overall, the upper tray produced a higher and narrower central dose region, whereas the lower tray produced a lower but wider plateau.

Based on the linearly interpolated 50% crossings, the X- and Y-axis FWHM values were 18.64 and 18.85 cm, respectively, for the upper tray and 29.05 and 28.14 cm, respectively, for the lower tray. Thus, the measured field widths were similar along the two principal axes within each tray, while the lower tray profiles were approximately 9–10 cm wider than the corresponding upper tray profiles.

The three-dimensional dose distributions further demonstrated the differences between the upper and lower tray positions. The upper tray produced a compact central high-dose region with steep changes at its boundaries (Fig. 2a (i-iii)). Its maximum measured dose was 1.05 Gy, with the maximum occurring at two neighboring grid positions. The lower tray produced a broader and relatively level high-dose region, with a maximum measured dose of 0.55 Gy (Fig. 2b (i-iii)). Based on the spatial extent of the high-dose plateaus, the approximate field dimensions were 20 × 20 cm for the upper tray and 30 × 30 cm for the lower tray. The different surface views consistently showed that the lower tray field covered a larger area than the upper tray field. Relative to these maximum measured doses, the fixed 0.02-Gy threshold used to define the 100% flatness window corresponded to approximately 1.9% for the upper tray and 3.6% for the lower tray.

Figure 2

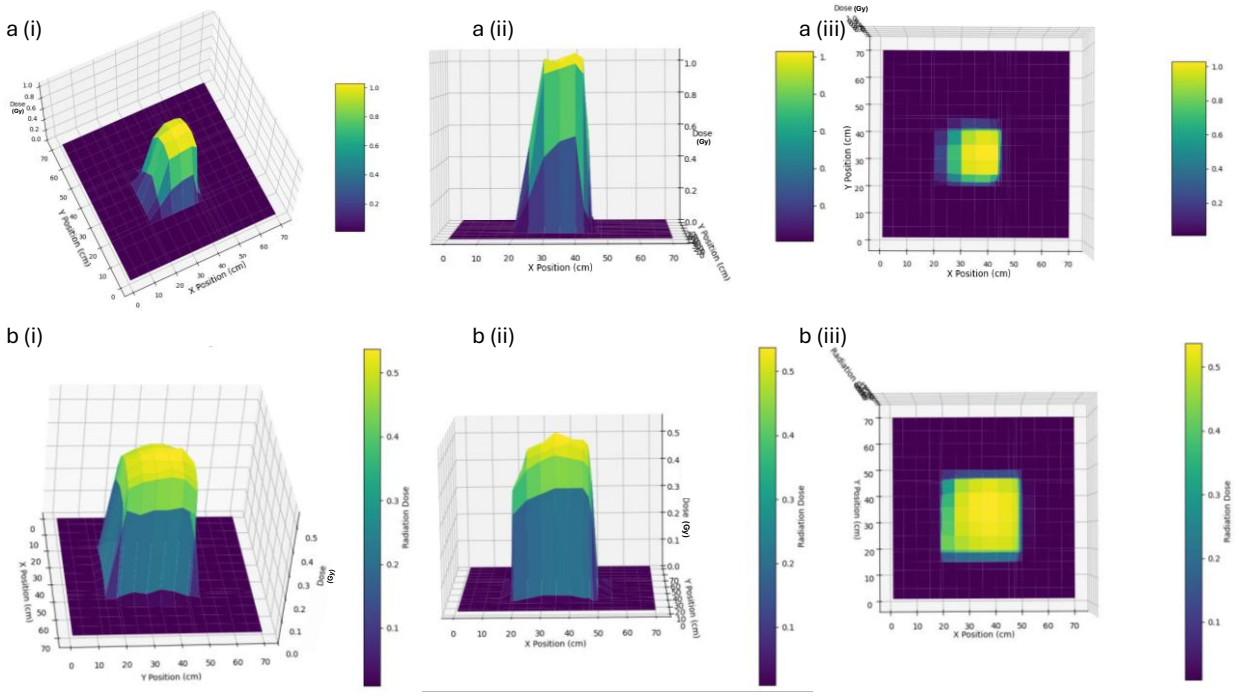


Fig. 2 Three-dimensional dose distributions at the upper and lower irradiation tray positions. Distributions for the (a) upper and (b) lower trays are displayed in oblique (i), lateral (ii), and top (iii) views. The viewing angles in a(i) and b(i) were selected independently to show the dose falloff at the lower field boundaries and are not intended as angle-matched comparisons. The X- and Y-axes are shown in centimeters, and the color bars indicate measured dose in Gy

The normalized isodose maps showed approximately square, nested contours surrounding the central high-dose regions (Fig. 3). The upper tray contours (Fig. 3 (i)) enclosed a smaller area and contained two neighboring positions with the same maximum recorded dose of 1.05 Gy at approximately (40, 30) cm and (40, 35) cm. These positions were tied at the retained numerical precision of 0.01 Gy and were therefore both marked as 100% dose locations. The lower tray (Fig. 3 (ii)) contours enclosed a larger area and contained one 100% position at approximately (35, 40) cm. Contour spacing was not uniform around all field boundaries, showing some spatial variation in the dose falloff. Because each map was normalized to its own maximum, the maps demonstrate differences in field shape and spatial extent but do not directly show the difference in absolute dose between the two trays.

Figure 3

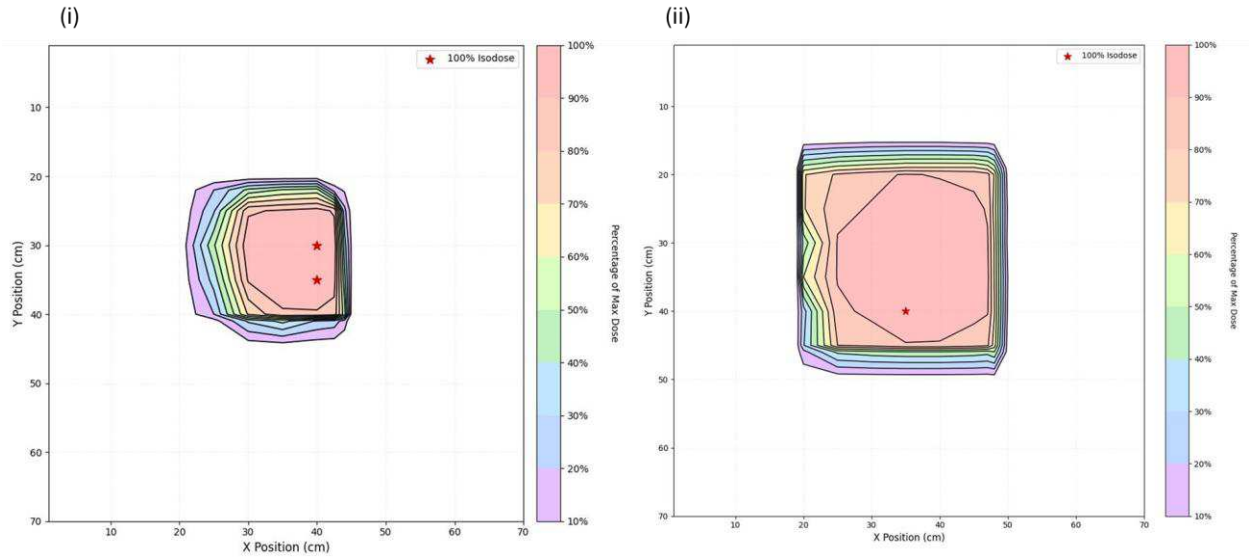


Fig. 3 Isodose contour maps. (a) Isodose contour maps for the upper (i) and lower (ii) irradiation platforms, plotted in the X–Y plane with dose levels shown from 10% to 100% in 10% increments. Each panel displays nested contour lines surrounding a central region marked by red star indicating the 100% isodose point. Axes are labeled in centimeters, and a color bar indicates the corresponding percentage dose levels

Beam flatness and symmetry varied with the evaluated field expansion window for both tray positions (Fig. 4). Along the X- and Y-axes, flatness values (Fig, 4 a(i), b(i)) changed comparatively little across the inner 20–60% windows and generally increased more markedly in the outer 80% and 100% windows. Symmetry (Fig. 4 a(ii), b(ii)) showed a similar pattern. Differences between opposing dose values were smaller within the inner 20–60% and became larger in the outer 80–100% windows. Thus, the principal changes in flatness and symmetry occurred when the evaluated regions extended beyond the central field and incorporated the field-boundary regions.

Figure 4

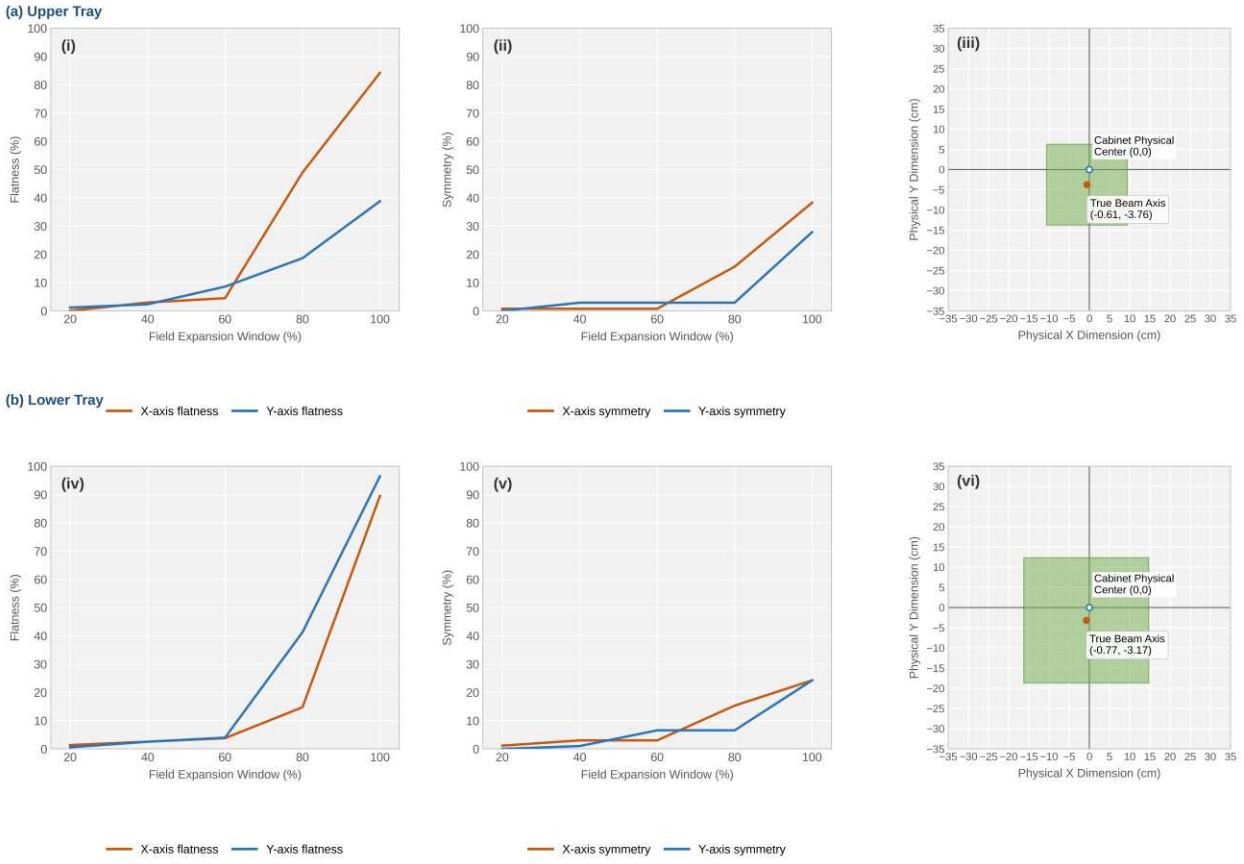


Fig. 4 Beam flatness, symmetry, and field alignment for the upper and lower irradiation trays of the X-RAD 320. (a) Upper tray and (b) lower tray. For each tray, (i) flatness and (ii) symmetry along the horizontal (X) and vertical (Y) profiles are plotted against the evaluated field expansion window (20–100%). The full width used for flatness was defined by the contiguous non-background dose region, whereas the full width used for symmetry was defined by the full width at half maximum. (iii) Centering plot showing the FWHM derived dose-based field center relative to the physical center of the cabinet, which was defined as the origin (0,0). The horizontal and vertical guide lines indicate the X- and Y-direction offsets, respectively. The shaded regions show the selected central reference areas of 20 × 20 cm for the upper tray and 30 × 30 cm for the lower tray. These regions were included as spatial references and do not represent acceptance tolerances

The field centering plots (Fig. 4a(iii), b(iii)) showed that the displacement was dominated by the negative Y component, which was −3.76 cm for the upper tray and −3.17 cm for the lower tray. The corresponding X components were −0.61 and −0.77 cm, respectively, and were comparable in magnitude to the uncorrected 0.65 cm distance between the chamber alignment point and reference point. The X-direction components should therefore be interpreted cautiously. The total centering discrepancies were approximately 3.8 and 3.3 cm for the upper and lower trays, respectively. The shaded regions were included as spatial references and were not used to classify the field centering as acceptable or unacceptable.

Descriptive analysis of the four separately irradiated corner films produced 12 gray-value profiles, comprising horizontal, vertical, and diagonal line profiles at each evaluated position (Fig. 5). Each profile showed a decrease in normalized gray value as the sampling line crossed from the lighter region into the darker irradiated region. The fitted Gompertz curves followed the overall sigmoidal transition and were used to identify the 80%, 50%, and 20% normalized gray-value positions. The 50% position provided an operational measure of the field edge location, while

the distance between the 80% and 20% positions described the film response transition width. The steepness and width of the transitions varied among the evaluated films and sampling directions. These differences are presented quantitatively in Table 1.

Figure 5

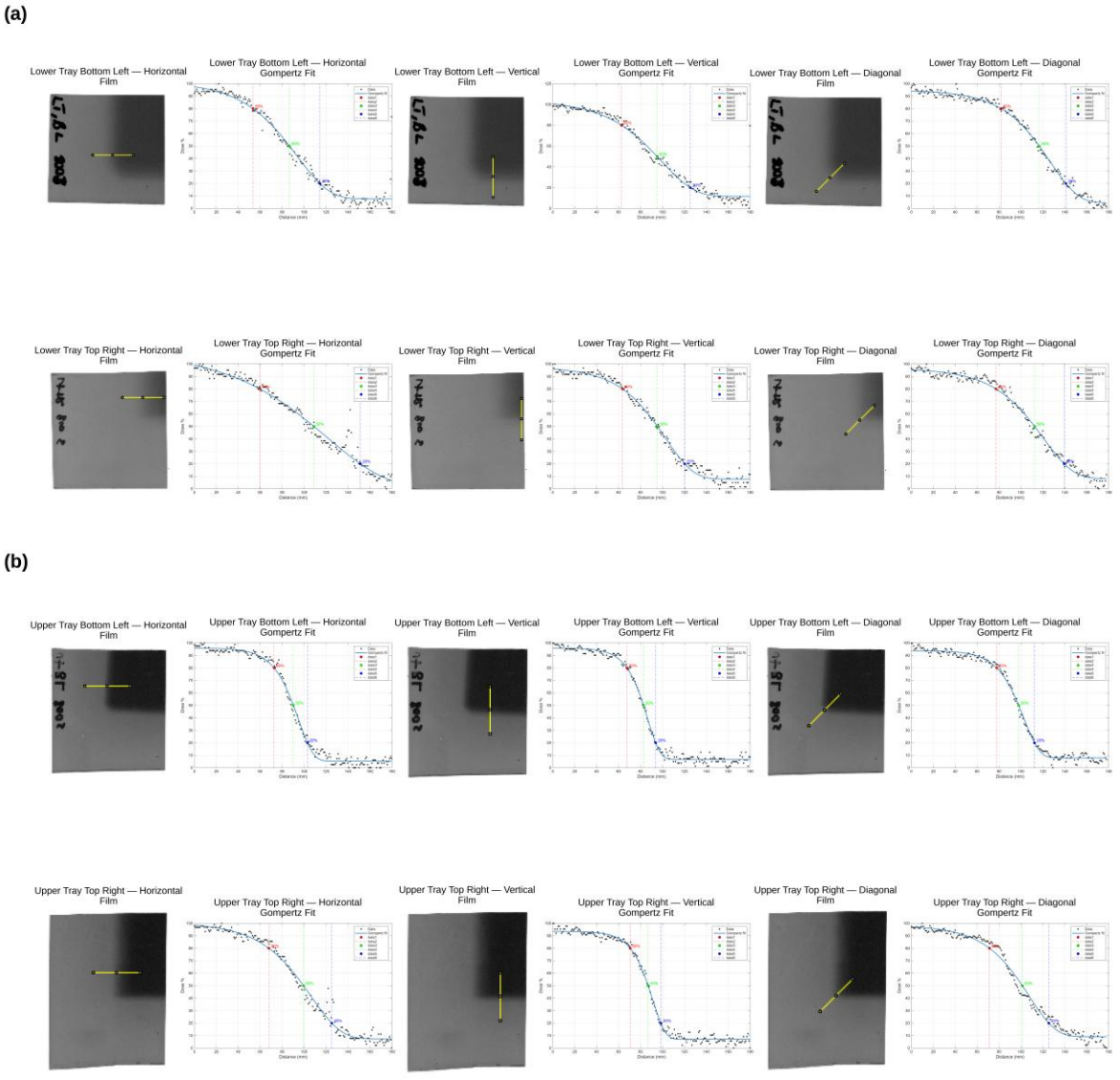


Fig. 5 Radiochromic film gray value profiles and Gompertz fits at the four evaluated corner positions. (a) Horizontal, vertical, and diagonal profiles obtained from the Lower Bottom-Left and Lower Top-Right films. (b) Corresponding profiles obtained from the Upper Bottom-Left and Upper Top-Right films. For each profile, the film image shows the position and orientation of the sampling line, and the adjacent graph shows the measured normalized gray values and fitted decreasing Gompertz curve. Red, green, and blue markers and vertical dashed lines identify the 80%, 50%, and 20% normalized gray value positions, respectively. Labels data1 - data6 corresponds to these threshold markers and guide lines. Dose (%) represent normalized film gray value. Distance (mm) represents pixel positions along the sampled profile, and physical distances were calculated using a conversion factor of 0.0847 mm per pixel. The 50% position was used as the operational field edge location, and the distance between the 80% and 20% positions described the film response transition width

Table 1 Profile-specific film response transition widths and local linear fit parameters for the four evaluated corner positions.

Corner	Direction	20–80% Transition Width (mm)	R^2	Slope (%/mm)
Upper Bottom-Left	Horizontal	2.27	0.970	-26.09
Upper Bottom-Left	Vertical	2.21	0.984	-26.30
Upper Bottom-Left	Diagonal	2.73	0.984	-23.87
Upper Top-Right	Horizontal	4.36	0.912	-13.12
Upper Top-Right	Vertical	2.13	0.968	-28.20
Upper Top-Right	Diagonal	4.13	0.925	-13.17
Lower Bottom-Left	Horizontal	5.25	0.964	-12.03
Lower Bottom-Left	Vertical	5.18	0.952	-11.58
Lower Bottom-Left	Diagonal	4.83	0.967	-12.85
Lower Top-Right	Horizontal	7.41	0.871	-7.49
Lower Top-Right	Vertical	4.15	0.961	-13.41
Lower Top-Right	Diagonal	5.13	0.970	-12.52

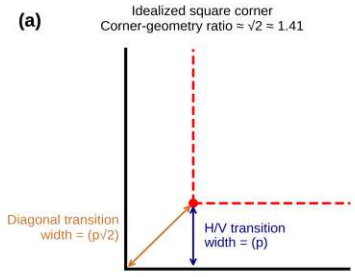
Horizontal, vertical, and diagonal profiles were obtained from the single film evaluated at each position. Transition width was defined as the distance between the 80% and 20% normalized gray value positions. R^2 describes the linear fit of the measured points within this transition, and slope describes the change in normalized gray value per millimeter. Negative slopes reflect the decrease in gray value from the lighter region toward the darker irradiated region

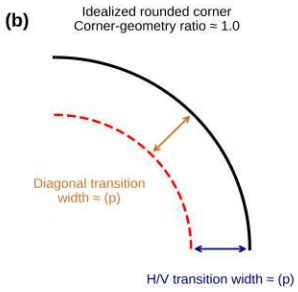
The measured 20 - 80% film response transition widths ranged from 2.13 to 7.41 mm across the four corner films and three sampling directions (Table 1). The narrowest transition was observed for the vertical profile of the Upper Top-Right film, whereas the widest transition was observed for the horizontal profile of the Lower Top-Right film. Measurements from the Upper Bottom-Left film ranged from 2.21 to 2.73 mm, and those from the Upper Top-Right film ranged from 2.13 to 4.36 mm. The corresponding values ranged from 4.83 to 5.25 mm for the Lower Bottom-Left film and from 4.15 to 7.41 mm for the Lower Top-Right film. Thus, the two lower tray films generally showed wider gray value transitions than the two upper tray films, although the measured width also varied with sampling direction. These observations were interpreted descriptively because only one film was evaluated at each position.

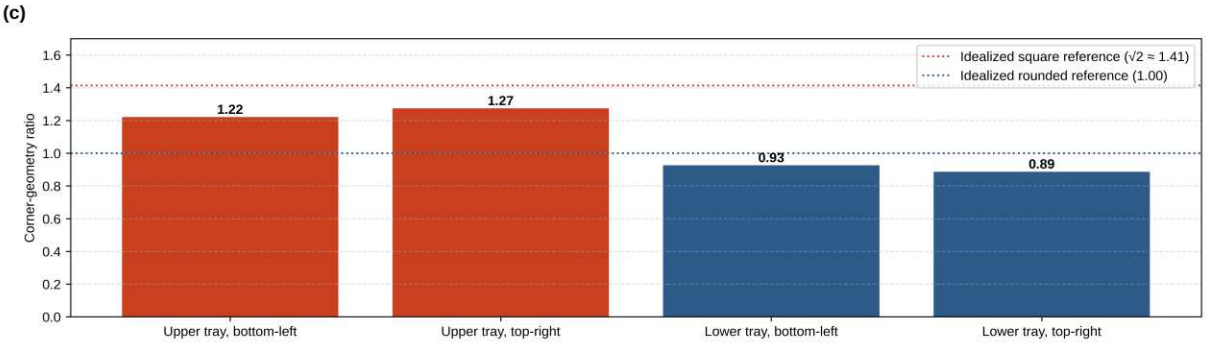
The profile-specific transition widths and local linear fit parameters are summarized in Table 1. The R^2 values ranged from 0.871 to 0.984, showing generally close agreement between the measured gray values and the local linear fits within the isolated 20–80% transitions. Profiles with narrower transition widths generally had larger absolute slopes. For example, the Upper Top-Right vertical profile had the narrowest measured transition width of 2.13 mm and an absolute slope of 28.20% per millimeter. In contrast, the Lower Top-Right horizontal profile had the widest transition width of 7.41 mm and the smallest absolute slope of 7.49% per millimeter. The three Lower Bottom-Left profiles showed similar transition widths of 4.83 - 5.25 mm and similar absolute slopes of 11.58 - 12.85% per millimeter. The individual measured data points and fitted regression lines underlying the slope and R^2 values in Table 1 are provided in Online Resource 3.

The exploratory corner geometry ratios differed descriptively among the four evaluated films (Fig. 6). The Lower Bottom-Left and Lower Top-Right ratios were 0.93 and 0.89, respectively (Fig. 6c) and were closer to the idealized rounded-corner reference of 1.00 than to the square-corner reference of 1.41 (Fig. 6a, b). The Upper Top-Right ratio was 1.27 and was closer to the square-corner reference. The Upper Bottom-Left ratio was 1.22 and fell nearly midway between the two reference values, although it was marginally closer to the square-corner reference. The two upper positions were therefore described as square-leaning and the two lower positions were described as arc-leaning. Circles constructed through their three 50% normalized gray value locations (Fig. 6d) produced descriptive radii of 5.69 mm for the Lower Bottom-Left position and 6.72 mm for the Lower Top-Right position.

Figure 6


(a)
Idealized square corner
Corner-geometry ratio ≈ √2 ≈ 1.41
Diagonal transition
width = (p√2)
H/V transition
width = (p)


(b)
Idealized rounded corner
Corner-geometry ratio ≈ 1.0
Diagonal transition
width ≈ (p)
H/V transition width ≈ (p)


(c)
Corner-geometry ratio
Idealized square reference (√2 ≈ 1.41)
Idealized rounded reference (1.00)
1.22
1.27
0.93
0.89
Upper tray, bottom-left
Upper tray, top-right
Lower tray, bottom-left
Lower tray, top-right

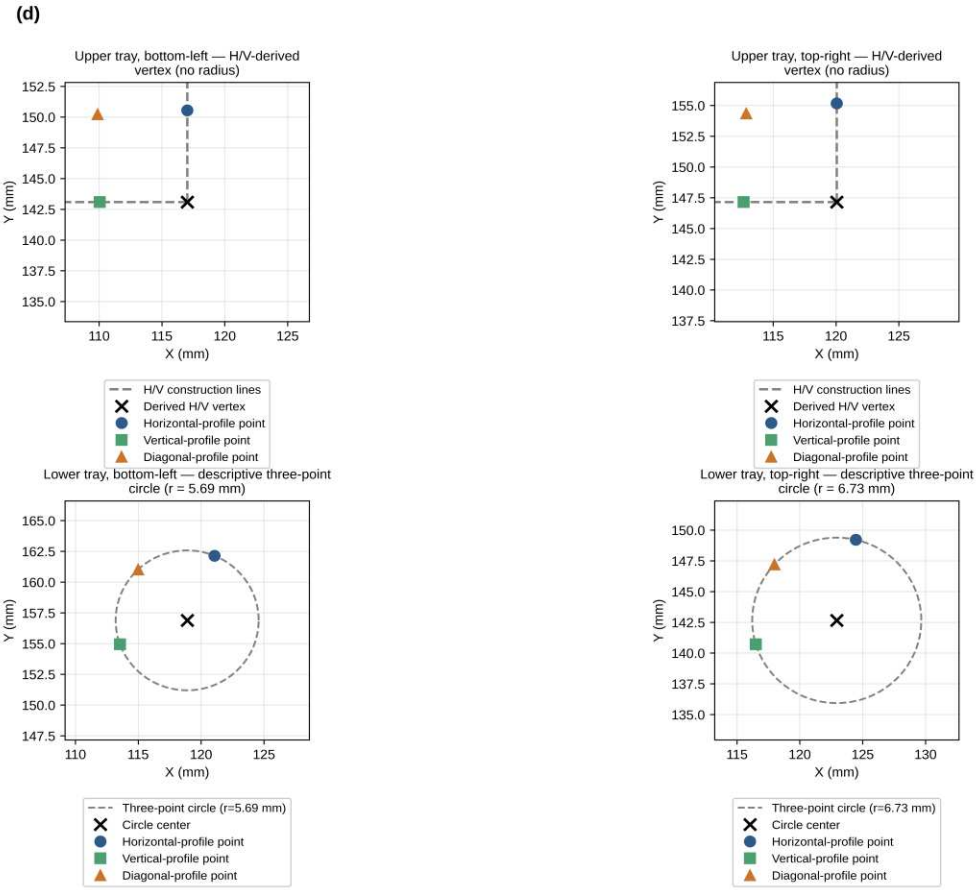

(d)
Upper tray, bottom-left — H/V-derived vertex (no radius)
Upper tray, top-right — H/V-derived vertex (no radius)
Lower tray, bottom-left — descriptive three-point circle (r = 5.69 mm)
Lower tray, top-right — descriptive three-point circle (r = 6.73 mm)
X (mm)
Y (mm)
H/V construction lines
Derived H/V vertex
Horizontal-profile point
Vertical-profile point
Diagonal-profile point
Three-point circle (r=5.69 mm)
Three-point circle (r=6.73 mm)
Circle center

Fig. 6 Exploratory comparison of the observed corner geometry with idealized square and rounded reference geometries. (a) Simplified geometry for an ideal sharp 90° corner, for which the diagonal-to-perpendicular transition width ratio approaches √2, or approximately 1.41. (b) Simplified geometry for an ideal rounded corner, for which the ratio approaches 1.00. (c) Measured diagonal transition width divided by the mean of the horizontal and vertical transition widths for each corner film, shown with the idealized square and rounded reference values. (d) Descriptive coordinate representations derived from the horizontal, vertical, and diagonal 50% normalized gray value locations. For the Upper Bottom-Left and Upper Top-Right tray positions, dashed horizontal and vertical guide lines connect their respective 50% locations to the derived H/V vertex, marked by a black ×. The diagonal 50% location was displayed independently and was not used to construct the vertex or assign a radius. Its separation from the derived vertex shows that the three locations did not form an exact idealized square corner. For the Lower Bottom-Left and Lower Top-Right tray positions, dotted circles pass through all three measured locations and have descriptive radii of 5.69 and 6.72 mm, respectively. The terms square-leaning and arc-leaning indicate proximity to the idealized reference values and do not represent definitive shape classifications. Each corner representation was derived from one separately irradiated film

DISCUSSION

Previous studies have established important dosimetric characteristics of the X-RAD 320. Azimi et al. (2015) evaluated field sizes from 4 × 4 to 20 × 20 cm² and examined output, depth dose, beam profiles, flatness, symmetry, and other beam characteristics using measurements and Monte Carlo simulations. Pidikiti et al. (2011) characterized an X-RAD 320 x-ray source fitted with a custom collimation system for image-guided stereotactic small-animal irradiation. Aldelaijan et al. (2013) used radiochromic film to examine dose delivery and beam profiles for biological specimens irradiated with an X-RAD 320. These studies demonstrate that beam characteristics depend on field size, measurement axis, irradiation geometry, and experimental setup. Although such factors may also have contributed to the patterns observed in the present study, the current measurements were not designed to identify a specific physical cause, such as the anode heel effect.

To our knowledge, the identified X-RAD 320 studies did not specifically combine two-dimensional chamber-grid measurements at two tray positions with field centering analysis and targeted examination of the locations where adjacent field edges intersect. The present study also used horizontal, vertical, and diagonal film profiles to describe local edge transitions and applied idealized geometric reference ratios and three-point circle construction to explore corner shape. These methods do not provide a validated classification of corner geometry or establish a physical radius of curvature, however, they provide a structured descriptive approach for examining peripheral field characteristics that may not be evident from conventional central-axis profiles, flatness measurements, or symmetry measurements alone.

Our central axis profiles results showed that tray position affected both the measured dose and the spatial extent of the radiation field (Fig. 1). The upper tray produced a central dose that was approximately twice that measured on the lower tray, but its high-dose plateau was narrower. In contrast, the lower tray produced a lower central dose over a wider region. This pattern was observed along both the X- and Y-axes. The findings are consistent with the different positions of the two measurement planes. The upper and lower trays were located approximately 19.5 and 46 cm from the X-ray tube housing, respectively. At the more distant lower tray, divergence of the X-ray beam would be expected to produce a wider field with a lower central intensity. The similar X- and Y-axis FWHM values within each tray indicate that the overall field width was comparable along the two principal axes. The upper tray Y-axis profile appeared to have a somewhat steeper transition than the corresponding X-axis profile.

The difference between the trays may not be attributed to distance alone. The lower tray was positioned closer to the cabinet floor, which may have increased the contribution of scattered and backscattered radiation at the measurement plane. The tray itself may also have provided some backscatter at both positions. Previous measurements with an X-RAD 320 showed that placing an ionization chamber over steel or solid-water backing increased the measured dose relative to an in-air arrangement (Azimi et al. 2015). Backscatter conditions can substantially affect dose measurements in orthovoltage irradiators (Chen et al. 2019). The installed filtration was unchanged between the two tray positions and therefore does not explain the observed differences through a change in filter setting. However, the reported distances were measured from the tube housing, and the possible effects of scatter or backscatter, cabinet geometry, and other system components were not evaluated separately. Therefore, these measurements should be considered an empirical characterization of the irradiator rather than a direct test of the inverse-square relationship. Nevertheless, the findings show that the two tray positions are not interchangeable. Selection of the tray should account for both the required dose and the dimensions of the experimental setup. The rapid dose reduction near the field boundaries also indicates that samples should be placed within the characterized central region and that the dose should be verified at the intended irradiation position.

The three-dimensional distributions (Fig. 2) extended the central-axis findings by showing how the dose varied across the complete measurement plane. The compact upper tray field and the broader lower tray field were consistent with the different tray positions. The upper tray was closer to the X-ray tube housing and received a higher dose over a smaller area. At the more distant lower tray, beam divergence produced a larger irradiated area with a lower maximum dose. This pattern was consistent with the higher and narrower upper tray profiles and the lower but wider lower tray profiles shown in Fig. 1.

The maximum doses in Fig. 2 were approximately one-half of the corresponding central-axis maxima in Fig. 1. This difference was consistent with the exposure times used in the two separate experiments. The three-dimensional measurements were obtained using 30-second exposures, whereas the Fig. 1 profiles were obtained using one-minute exposures. At corresponding coordinate positions, the profiles extracted from the two-dimensional dose matrices generally agreed with the Fig. 1 profiles in dose magnitude, plateau extent, and approximate field edge location after accounting for the different exposure times. The agreement in the relative differences between the trays supports the overall consistency of the measurements, although the two experiments should not be treated as a direct quantitative comparison.

The two neighboring upper tray positions with the same maximum dose most likely represented a small region of similar dose combined with the spacing and numerical precision of the measurements. They should not be interpreted as two separate beam centers. The estimated 20 × 20 cm and 30 × 30 cm dimensions describe the approximate spatial extent of the high dose plateaus. They were not calculated from the 50% dose points or the full width at half maximum and should therefore not be considered exact field dimensions. The approximately square contour shape at both tray positions was determined from the present isodose maps. The approximately 20 × 20 cm upper-tray high-dose plateau was comparable in scale to the largest square field evaluated by Azimi et al (Azimi et al. 2015). In contrast, the approximately 30 × 30 cm lower-tray plateau exceeded the field-size range examined in that study and was therefore not interpreted as being directly supported by the Azimi et al. comparison. Its larger extent was instead interpreted from the present measurements as being consistent with greater geometric projection at the more distant measurement plane. Small departures from an ideal square boundary may reflect the combined effects of beam divergence, focal spot geometry, collimator alignment, and scatter, and these contributions were not evaluated separately in our study. The steep dose changes around the upper tray plateau also indicate that dose delivery at this position may be more sensitive to sample placement near the field boundaries. The wider lower tray plateau provided a larger irradiation area, but at a lower dose. These findings demonstrate the importance of selecting the tray and sample position according to both the required dose and the dimensions of the experimental setup.

The isodose maps (Fig. 3) confirmed that the spatial shape of the field differed between the two tray positions. The smaller contours on the upper tray and the larger contours on the lower tray were consistent with the three-dimensional distributions shown in Fig. 2. The approximately square contour shape reflected the overall geometry of the irradiated regions. The closer contour spacing along the right and lower boundaries of the upper tray field suggested a more rapid local dose falloff in these regions. This variation was less apparent in Fig. 1 because the one-dimensional profiles represented only the central X- and Y-axes, whereas the isodose map included measurements across the complete two-dimensional plane. The wider lower tray contours were also consistent with greater beam divergence at the more distant measurement plane.

The two neighboring 100% positions on the upper tray most likely represented a small region with similar measured doses, together with the spacing and numerical precision of the measurements. They should not be interpreted as two separate beam centers or distinct hot spots as previously mentioned. Similarly, the single 100% position on the lower tray identifies the highest sampled position but does not, by itself, define the center of the complete field. The field centering calculations in Fig. 4 used the positions of the interpolated 50% dose crossings rather than the location of a single maximum measurement.

The predominance of the negative Y-direction displacement at both tray positions is consistent with, but does not prove, a systematic directional offset between the dose-defined field center and the physical center of the cabinet. The smaller X-direction components were comparable in magnitude to the uncorrected 6.5-mm distance between the chamber alignment point and reference point and cannot be interpreted as evidence of X-axis miscentering. Possible contributors to the dominant Y-direction displacement include the relative alignment of the X-ray source, collimator, tray, and cabinet coordinate system, as well as axis dependent dose falloff that could influence the interpolated 50% crossing positions. Because these factors were not evaluated independently, the present measurements establish the direction and magnitude of the displacement but do not identify its cause or demonstrate a specific mechanical defect.

The unequal spacing between contours around the field boundaries showed that the dose did not decrease at the same rate in every direction. This finding demonstrates the value of two-dimensional mapping because a single central axis profile cannot fully describe spatial variation around the field. However, the contour boundaries were interpolated between measured grid positions. Small differences in contour shape or spacing should therefore be interpreted cautiously and should not be considered evidence of a specific equipment defect. Samples placed near the field boundaries may be more sensitive to small differences in position than samples placed within the central region.

Because each map was normalized independently, the same percentage or color did not represent the same absolute dose on the two trays. For example, the 100% contour represented 1.05 Gy on the upper tray but 0.55 Gy on the lower tray. The normalized maps are therefore useful for comparing field shape, relative dose falloff, and spatial coverage. The absolute dose difference between the trays is better demonstrated by the three-dimensional distributions in Fig. 2.

The flatness (Fig. 4a,b(i)) and symmetry (Fig. 4a,b(ii)) results showed that the central portions of both fields were more uniform than their outer portions. Since the evaluation windows were nested and cumulative, the flatness and maximum symmetry values could only remain unchanged or increase as the window expanded. The informative finding was therefore not simply the nondecreasing direction of the trend, but that the values changed comparatively little through the 60% window and increased mainly in the 80% and 100% windows, when the evaluated regions incorporated the field boundaries. The large flatness values in the outer windows reflect the inclusion of regions of rapid dose falloff and should not be interpreted as poor uniformity throughout the central irradiated region. The anode heel effect is a possible contributor because axis-dependent beam uniformity has previously been reported for the X-RAD 320 (Azimi et al. 2015). However, the anode–cathode orientation and the contribution of the heel effect were not evaluated separately in the present study. We therefore describe it as a possible contributing factor rather than the confirmed cause of the observed difference. Nevertheless, these results are consistent with the three-dimensional distributions and the unequal contour spacing observed around the field edges in Figs. 2 and 3.

The symmetry analysis also showed larger differences between opposing dose values as the evaluated window approached the field boundaries. The larger symmetry differences in the outer windows occurred as the paired evaluation positions entered regions of steep dose gradient, where a small spatial difference could produce a relatively large dose difference. Some symmetry values remained unchanged across adjacent windows because the same maximum pairwise difference was retained in more than one cumulative window. Since the calculations used selected expansion windows, the reported flatness and symmetry values should be considered descriptive. They should not be compared directly with equipment acceptance limits that use different field definitions or measurement conditions.

From a practical standpoint, the findings indicate that experimental samples should be positioned relative to the characterized dose field rather than relying only on the physical cabinet center or crosshair. The shaded regions provide spatial references for this purpose but do not represent acceptance tolerances.

The film profiles (Fig. 5) provided a detailed, descriptive view of the local field edge transitions. All 12 profiles showed a gradual sigmoidal change from the lighter region to the darker irradiated region. The Gompertz function provided a consistent empirical method for locating the 80%, 50%, and 20% gray value positions across profiles with different shapes. The function was used as an interpolation method and was not intended to represent the physical processes responsible for the dose distribution.

The 50% position provided a common operational definition of the local field edge. Similarly, the distance between the 80% and 20% positions provided a common measure of the film response transition width. However, these values were obtained from normalized grayscale measurements rather than a calibration of film response to absorbed dose. Therefore, the 20–80% interval should not be interpreted as a dosimetric gray value transition or directly compared with a gray value transition calculated from percentage absorbed dose.

The observed differences among corners and sampling directions may reflect variation in the local shape and orientation of the field boundary. A horizontal, vertical, or diagonal line may cross an oblique or curved boundary at a different angle, which can change the apparent transition width even when the underlying boundary is unchanged. Film positioning, scan alignment, scanner response, and image normalization may also have contributed to the observed differences. The differences therefore cannot be attributed solely to variation in the radiation field.

Only one film was evaluated at each corner, and each film was obtained during a separate irradiation. In addition, the three directional profiles from each film were obtained from the same film and were not independent replicates. Consequently, the present measurements cannot establish the repeatability of the corner profiles or support statistical comparisons among corners and sampling directions. Moreover, because the films were irradiated directly on the tray, the measured gray value transitions may have included contributions from scatter and backscatter from the tray. No separate support or backscatter condition was evaluated, and the magnitude of this contribution could not be determined from the present measurements. Nevertheless, the analyses provided a consistent descriptive assessment of the four evaluated field edges and formed the basis for the transition width comparisons summarized in Table 1.

The transition width measurements (Table 1) provided quantitative support for the differences observed among the film profiles in Fig. 5. The two lower tray films generally had wider normalized gray value transitions than the two upper tray films. This pattern was consistent with the broader lower tray field observed in the chamber-based profiles and dose maps. The generally wider lower-tray transitions were qualitatively consistent with increased geometric spreading at the longer source-to-film distance. However, the focal-spot-to-film distances, focal-spot size, and internal collimator geometry were not independently measured and therefore, a quantitative geometric-penumbra calculation was not performed, and the specific contributions of these factors could not be determined.

Transition width also varied with sampling direction (Table 1), particularly for the Upper Top-Right and Lower Top-Right films. These differences may reflect the local shape and orientation of the field boundary. A sampling line that

crosses a curved or oblique boundary at an angle can produce a wider apparent transition than a line that crosses the boundary more directly. Therefore, differences among the horizontal, vertical, and diagonal profiles should not be interpreted as evidence of directional differences in the radiation field alone.

The local linear fits (Table 1 and Online Resource 3) provided a simple measure of the rate of gray value change within the 20–80% transition. Narrower transitions generally produced larger absolute slopes because the same 60 percentage point change occurred over a shorter distance. Consequently, transition width and absolute slope represent related descriptions of the same film response and should not be considered independent findings. The R^2 values showed that a linear approximation described the selected transition regions reasonably well, although the profiles retained some curvature and measurement variation.

The corner-film findings should be interpreted as exploratory. Since only two diagonally opposed corners were evaluated at each tray position, and one separately irradiated film was available for each selected corner, the apparent difference between the upper and lower tray films remain descriptive. Consequently, the measured transition widths and exploratory geometry classifications cannot be generalized to the unsampled corners or used to establish the reproducibility of corner geometry across repeated irradiations. Nevertheless, Table 1 provide a consistent quantitative summary of the local film response transitions and identify patterns that can be examined in future studies using repeated all corner exposures and calibrated film dosimetry.

The exploratory ratios suggested differences in corner geometry among the four evaluated films (Fig. 6). The two lower tray positions were closer to the idealized rounded corner reference, whereas the two upper tray positions were closer to the square corner reference (Fig. 6 a, b, c). These findings suggest that the field boundary may not be represented fully by nominal square field dimensions alone, particularly near the corners. Differences in projected corner geometry could be influenced by beam divergence, collimator geometry, alignment, position of x-ray target, and the position of the film within the cabinet. The present measurements cannot distinguish among these possible explanations.

The rounded and square corner reference ratios were idealized geometric values and were not validated classification thresholds. The terms “arc-leaning” and “square-leaning” should therefore be interpreted as relative descriptive labels rather than definitive classifications. The visual appearance of the film images qualitatively supported these descriptions, with the lower tray corners appearing more curved and the upper tray corners appearing more angular (Fig. 5). The Upper Bottom-Left ratio of 1.22 was intermediate between the two reference values and only marginally closer to the square-corner reference. Since measurement uncertainty and sensitivity to sampling line placement were not quantified, its square-leaning designation should be regarded as borderline. More generally, this reference ratio model represents a first-order exploratory approach because it did not explicitly account for the two-dimensional overlap of adjacent field-edge transition regions or quantify sensitivity to localization of the corner and small changes in sampling-line placement, particularly for the diagonal profile. These effects should be evaluated in future studies using replicated full-field film measurements.

The visible curvature of the two lower tray corners on the film supported their exploratory representation as arcs. The radii calculated for the two arc-leaning positions (Fig. 6d) provided estimates of the scale of the apparent corner curvature. However, since a circle can be constructed through any three non-collinear points, the resulting radii therefore do not irrefutably demonstrate that the complete field boundary followed a circular arc. Nevertheless, this exploratory approach provides a descriptive assessment of local corner geometry and may help guide more detailed evaluation of field boundaries in future replicated film measurements.

Square-leaning and arc-leaning describe the spatial geometry of the sampled corner, whereas the 20–80% normalized gray value transition width describes edge sharpness. We note that perfectly abrupt boundaries are not expected because of finite focal spot size, source–collimator geometry, beam divergence, and scatter. Narrower transitions

would generally be advantageous for small field conformal irradiation because they improve spatial selectivity, consistent with the importance of high gradient, accurately localized fields in the custom-collimated stereotactic system described by Pidikiti et al. However, rounded corners are not necessarily disadvantageous, and our exploratory film measurements do not establish the unit's suitability for stereotactic irradiation.

CONCLUSION

This study characterized the central and peripheral radiation field properties of an X-RAD 320 at two irradiation tray positions by combining chamber-grid and radiochromic film measurements. The upper tray produced a higher and more compact central dose region, whereas the lower tray produced a lower but broader field. Flatness and symmetry changed comparatively little across the inner 20–60% evaluation windows and increased primarily in the outer 80% and 100% windows as the evaluated regions incorporated the field boundaries. The film measurements showed descriptive variation in gray value transition width and suggested square-leaning upper corners and arc-leaning lower corners. These findings demonstrate the importance of considering tray position and specimen placement when planning and reproducing irradiations, particularly near field edges and corners. Since only one separately irradiated film was examined at each corner and the film values were not calibrated to absorbed dose, replicated and dose calibrated measurements are needed to confirm the observed corner patterns.

Because the films were not calibrated to absorbed dose and the maximum chamber-measured doses differed by approximately a factor of two between the tray positions, the normalized gray value transitions may have corresponded to different portions of the EBT-XD dose–response curve. Normalization does not eliminate this potential dose-response effect, and its contribution to the apparent transition-width differences between the upper- and lower-tray films could not be quantified in the present study.

STATEMENTS AND DECLARATIONS

Acknowledgements: The authors wish to thank the program director, Dr. Amy Brady, and other faculty in the Nuclear Medicine and Molecular Imaging Sciences Program for facilitating the smooth conduct of this research. During manuscript development, generative AI technologies were utilized exclusively for editorial assistance, including language polishing, grammatical corrections, and enhancement of readability. The scientific content, study design, data generation, analyses, interpretation, and conclusions were conceived and completed by the authors. The authors independently verified all content and references and accept complete responsibility for the final published work.

Author contributions: Remo George conceived and designed the study and reviewed and edited the manuscript. Bashayr Alotaibi performed the primary experimental measurements. Will Ren performed the film scanning, ImageJ processing, and corner geometry analyses. Bonny Dikago performed the Gompertz curve fitting. Will Ren and Bonny Dikago prepared the original manuscript draft. Ara Alexandrian conducted the initial film experiments that contributed to the development of the field edge characterization approach. Joseph Steiner critically reviewed and revised the manuscript. All authors read and approved the final manuscript.

Funding: Research reported in this publication was supported by faculty IRP funds from the Chair of the University of Alabama at Birmingham, department of Clinical and Diagnostic Sciences, and material support from the UAB Nuclear Medicine and Molecular Imaging Sciences program, along with grant from the National Center for Research Resources Research Facility Improvement, 1 G20RR022807-01, for the UAB X-RAD 320 irradiator. Radiochromic films used in this research were a kind gift from Dr. Ara Alexandrian of the UAB Health Physics program.

Data availability: The processed measurement data, calculation workbooks, and available scanned film images supporting the findings of this study are available from the corresponding author upon reasonable request. The archived chamber datasets contain the averaged values used in the analyses.

Competing interests: None

Ethics approval: Not applicable.

Consent to participate: Not applicable.

Consent for publication: Not applicable.

Supplementary Information:

Online Resource 1 Python script used to generate the three-dimensional dose surface plots presented in Fig. 2.

Online Resource 2 Python script used to generate the isodose contour maps presented in Fig. 3.

Online Resource 3 Supplementary Fig. S1. Local linear fits of the 20 - 80% normalized gray value transitions for the four evaluated corner films. The figure presents the measured profile points and ordinary least-squares regression lines for the horizontal, vertical, and diagonal profiles at each evaluated position. The corresponding slopes, coefficients of determination, and transition widths are reported in Table 1.

REFERENCES

Aldelaijan S, Nobah A, Alsbeih G, Moftah B, Aldahlawi I, Alzahrany A, Tomic N, Devic S (2013) Dosimetry of biological irradiations using radiochromic films. Phys Med Biol 58 (10):3177–3189. doi:10.1088/0031-9155/58/10/3177

Azimi R, Alaei P, Spezi E, Hui SK (2015) Characterization of an orthovoltage biological irradiator used for radiobiological research. J Radiat Res 56 (3):485–492. doi:10.1093/jrr/rru129

Bucher M, Trinkl S, Endesfelder D, Weiss T, Gomolka M, Patzold J, Lechel U, Roessler U, de Las Heras Gala H, Moertl S, Giussani A (2021) Radiation field and dose inhomogeneities using an X-ray cabinet in radiation biology research. Med Phys 48 (12):8140–8151. doi:10.1002/mp.15297

Chen Q, Molloy J, Izumi T, Sterpin E (2019) Impact of backscatter material thickness on the depth dose of orthovoltage irradiators for radiobiology research. Phys Med Biol 64 (5):055001. doi:10.1088/1361-6560/ab0120

Desrosiers M, DeWerd L, Deye J, Lindsay P, Murphy MK, Mitch M, Macchiarini F, Stojadinovic S, Stone H (2013) The Importance of Dosimetry Standardization in Radiobiology. J Res Natl Inst Stand Technol 118:403–418. doi:10.6028/jres.118.021

Khan FM, Gibbons JP (2014) The physics of radiation therapy. EBSCO Academic Collection., 5th edn. Lippincott Williams & Wilkins, Philadelphia

Mujahid A, Alotaibi B, DeMellier C, Gallegos C, Sherwani M, Alexandrian A, Sorace A, Brady A, George R (2025) Characterization of Cutaneous Radiation Syndrome in a Mouse Model Using [18 F]F- Fluorodeoxyglucose Positron Emission Tomography. Health Phys 129 (3):204–213. doi:10.1097/HP.0000000000001947

Niroomand-Rad A, Chiu-Tsao ST, Grams MP, Lewis DF, Soares CG, Van Battum LJ, Das IJ, Trichter S, Kissick MW, Massillon-Jl G, Alvarez PE, Chan MF (2020) Report of AAPM Task Group 235 Radiochromic Film Dosimetry: An Update to TG-55. Med Phys 47 (12):5986–6025. doi:10.1002/mp.14497

Pidikiti R, Stojadinovic S, Speiser M, Song KH, Hager F, Saha D, Solberg TD (2011) Dosimetric characterization of an image-guided stereotactic small animal irradiator. Phys Med Biol 56 (8):2585–2599. doi:10.1088/0031-9155/56/8/016

Precision X-Ray, Inc. (2022) X-Rad320: Product data (Datasheet Rev. 04). Precision X-Ray, Inc. https://bcf.technion.ac.il/wp-content/uploads/2022/11/X-Rad320.pdf.

Saikkonen A, Niemela J, Sipila P, Keyrilainen J (2019) Commissioning of the MultiRad 350 cell and small animal x-ray irradiation system. Phys Med 59:107–111. doi:10.1016/j.ejmp.2019.03.004

Trompier F, DeWerd LA, Poirier Y, Dos Santos M, Sheng K, Kunugi KA, Winters TA, DiCarlo AL, Satyamitra M (2024) Minimum reporting standards should be expected for preclinical radiobiology irradiators and dosimetry in the published literature. Int J Radiat Biol 100 (1):1–6. doi:10.1080/09553002.2023.2250848

Supplementary Files

This is a list of supplementary files associated with this preprint. Click to download.

- SI.pdf